




The study of optical, structural and magnetic properties of Cu-doped ZnO nanoparticles

Mahendra Kumar Gora^{1,*} , Arvind Kumar¹, Sanjay Kumar¹, Jagdish Nehra¹, Banwari Lal Choudhary², Satya Narain Dolia^{1,1}, and Rishi Kumar Singhal^{1,1}

¹Department of Physics, University of Rajasthan, Jaipur, Rajasthan 302004, India

²Department of Physics, Bansathali Vidhyapith, Banasthali, Rajasthan 304022, India

Received: 28 September 2022

Accepted: 30 November 2022

Published online:
25 January 2023

© The Author(s), under exclusive licence to Springer Science+Business Media, LLC, part of Springer Nature 2023

ABSTRACT

Zinc oxide is a multifunctional material with important applications in areas like electronics, optoelectronics, sensors and photocatalysis. In the present work, the Cu-doped ZnO (Cu = 0%, 2% and 5%) nanoparticles have been synthesized and investigated using various techniques like XRD, SEM, XPS, PL and UV spectroscopic measurements. The study is aimed at exploring the mechanism of room-temperature ferromagnetism in these dilute magnetic semiconductors, which has been a mystery for a long time. The X-ray diffraction patterns revealed the hexagonal wurtzite crystal structure of the $P6_3mc$ space group and an average crystalline size of 26 nm to 32 nm. The morphology has been analyzed using SEM images, which depict irregular grain size distribution and agglomerated spheroid-like particle structure. The X-ray photoelectron spectroscopy (XPS) findings exhibited the inducement of remarkable oxygen vacancies (V_o) with Cu doping. The 2% Cu-doped sample shows the maximum value of the oxygen vacancies. The magnetization measurements reveal weak ferromagnetism in the pure ZnO sample, whereas the Cu-doped ZnO nanocrystalline samples show remarkable room temperature ferromagnetism (RTFM). The 2% Cu-doped sample depicts the highest value of saturation magnetization. The UV spectroscopy indicates that the band gap is reduced upon Cu doping; the value of E_g is found to be the lowest (2.96 eV) for the 2% Cu-doped sample. The Photoluminescence (PL) spectroscopy indicates the presence of defect-related states, which are found to be the maximum for the 2% Cu-doped sample, in good agreement with the XPS results. The induced magnetization in the Cu-doped nano-crystalline samples is found to show a direct relationship with the oxygen vacancies and is proposed to be caused by the exchange interactions between the Cu^{2+} ions and the oxygen vacancies. The inducement of ferromagnetism in ZnO renders it a potential system for spintronic devices. The key benefits of spintronic devices are their compact size,

Address correspondence to E-mail: gora.phy@gmail.com

excellent luminous efficiency, ecologically benign composition, long persistence and potential energy savings.

1 Introduction

The dilute magnetic semiconductors (DMS) have attracted tremendous attention from researchers because of their potential use in spintronic devices with integrated magnetic and electronic properties [1–3]. The DMS with the magnetic elements' data storage potentiality may be achieved in a single material via spintronic appliances. A valuable method for combining electric charges and spins to enhance their characteristics, such as magneto-optical properties [4], is the doping of transition-metal (TM) elements in the host semiconductors. Innovative devices, circuits and spin transistors can be created using these features. For such devices, the average spin of a group of electrons is required, as indicated by magnetization. Consequently, the magnetic characteristics are crucial to DMS systems and achieving stable RTFM in them for their practical applications is a challenge [5]. The literature reveals that the various applications of ZnO can be enhanced by doping several TM elements like Cu, Fe, Ni, Co, Mn and Cr etc. [6–9].

When the TM elements are doped into ZnO lattice they bring about remarkable improvements in its electrical, magnetic and optical properties, which help in developing new electronic and optoelectronic devices [10, 11]. The RTFM in TM-doped ZnO nanoparticles has been universally reported in the last decade. In numerous experiments, the RTFM was observed by doping TM elements with partially filled d electrons into ZnO lattice [12]. Nevertheless, RTFM's origin abides debatable because it is unclear whether the exhibited ferromagnetism is entirely an intrinsic characteristic or spurred on by the TM ions [13]. Metal clusters, vacancy clusters [14], secondary oxide phases [15] and magnetic contamination [16] are possible explanations for the genesis of ferromagnetic properties and coupling mechanisms. The TM-doped RTFM was theoretically reported by Dietl et al. [17]. Further research into the field has revealed that the doping elements and the synthesis techniques affect their magnetic characteristics a great deal [18–21].

The first-principal calculations demonstrate that Cu which is a diamagnetic and non-ferromagnetic element, when doped in the ZnO can induce ferromagnetism in it [22, 23]. Being in the + 2 valence states the Cu creates additional acceptor and donor levels in the band structure of the Cu-doped ZnO [24]. Sharma et al. [25] synthesized the Cu-doped ZnO nanorods with the Cu²⁺ (1–10%) doping percentage via the hydrothermal process. They observed strong RTFM behavior in the prepared nanorods, but with a higher doping concentration of Cu, the ferromagnetic characteristics were found to get suppressed and paramagnetic behavior started appearing. The increased antiferromagnetic interaction between nearby Cu-Cu ions was ascribed to the reduction in ferromagnetism with the growing Cu doping percentage. Yldrm et al. [26] studied ZnO: Cu nanoparticles with distinct concentrations of Cu incorporation (1.25%, 2.5% and 5%) prepared via the precipitation method and observed RTFM properties in them. The magnetization was reported to increase with increasing Cu concentrations because of the shrinking of the band gap, implying that RTFM behavior is an inherent feature of ZnO: Cu nanoparticles. Wang et al. [27] explored the RTFM and PL properties of lightly Cu-doped ZnO nanocrystalline with varying Cu doping amounts, which were synthesized via an easy solution technique. Their XPS and PL results showed that the oxygen vacancies were plentiful in the lightly Cu-doped ZnO nanocrystalline and the dispensation of these flaws existed almost stationary. The saturation magnetization was highest at 0.25% Cu doping; beyond that, it decreased with further doping. Their findings suggest that the Cu ions can increase long-range ferromagnetic ordering at very low concentrations. Still, they may also create antiferromagnetic 'Cu⁺-V_o-Cu²⁺' pairs even at meager Cu-doping amounts.

The above factors make it possible to learn more about the coupling process and the origin of the ferromagnetic characteristics of DMS systems, which are still open for debate [28]. Despite a lot of efforts, the mechanism of RTFM's genesis in DMS systems remains a mystery.

DMS nanocrystalline systems are believed to have a longer coherence time, which can furnish a route for enhancing the spin lifetime for useful spintronics devices [29–31]. Although metallic copper is not magnetic, its oxides, such as cupric oxide (CuO) and cuprous oxide (Cu₂O), are also not ferromagnetic. Still, the Cu-doped ZnO shows ferromagnetic behavior and is defined to be an important DMS system.

The ferromagnetic characteristics are found to have been manipulated by hybridization of the empty 3d states of TM ions with the ZnO donor states at the Fermi level. The generation of oxygen vacancies (V_o), have been found to be crucial for producing ferromagnetism in DMS systems [31]. The Cu is the most promising dopant amongst the several TMs due to its ionic radii Cu²⁺ (0.73 Å) being nearly identical to the Zn²⁺ (0.74 Å); its electronic properties are also similar and easily substitutable, making it a viable option for doping in ZnO [32]. Furthermore, the Cu plays a crucial role in the formation of localized impurity levels in the ZnO crystal lattice [33, 34].

In the current study, we have prepared the Cu-doped ZnO nanocrystalline (Cu = 0%, 2% and 5%) samples using the co-precipitation technique. The XRD pattern depicts the hexagonal wurtzite structure for all the nanocrystalline samples. The morphology of the prepared samples is studied by SEM images. The XPS findings reveal that the 2% Cu-doped ZnO sample shows more oxygen vacancies than the pure ZnO and the 5% Cu-doped ZnO nanocrystalline samples. The PL spectroscopy findings agree well with the XPS results. The UV visible spectroscopy findings exhibit that the band gap is reduced with Cu doping. It is observed that the reduction in E_g for the 2% Cu-doped sample is more than the pure ZnO and the 5% Cu-doped ZnO nanoparticles. SQUID measurements have been used to analyze the magnetic properties of the Cu-doped ZnO nanoparticles and the 2% Cu-doped sample exhibited the maximum saturation magnetization and also the maximum density of oxygen vacancies. It is worth mentioning that ZnO besides being a multifunctional system for several applications in electronics, optoelectronics, sensors, and photocatalysis, has also been found to play an important role in important environmental issues, like controlling electromagnetic pollution through high-efficiency electromagnetic wave absorption materials (EWAMs) and the doping technology due to its hollow structure. This has been

summarized in recent works [35–37]. Liang et al. [38, 39] showed the importance of Cu nanoparticles and explored the Cu-NC system (i.e., the N-doped carbon) in this regard. The modulation of morphology, composition, interface, defects, and conductivity were explored by them by adjusting the ratio of copper salt to the reducing agent chitosan. The appearance of twin boundaries (TBs) was found to resist the oxidation of metal Cu⁰, keeping the electric conductivity of Cu⁰ nanoparticles high and enhancing the conduction loss, which provides a boost for electromagnetic wave dissipation.

2 Experimental section

2.1 Sample preparation

The Cu-doped ZnO nanocrystalline (Cu = 0%, 2% and 5%) samples have been synthesized via the co-precipitation method. High purity analytical grade zinc acetate dihydrate [Zn(CH₃CO)₂·2H₂O], copper acetate monohydrate [Cu(CH₃CO)₂·H₂O] and potassium hydroxide [KOH] (Make; Sigma-Aldrich) were utilized as the primary materials. The stoichiometric amounts of [Zn(CH₃COO)₂·2H₂O] and (0%, 2% and 5%) dopant [Cu(CH₃COO)₂·H₂O] were dissolved in deionized water and converted into an aqueous solution. Both the solutions were mixed slowly with steady stirring to get a homogeneous solution. The aqueous solution was heated to 60 °C with continuous churning. The KOH 1 M solution was poured drop by drop to control the pH value close to 11 under constant stirring. The solution was maintained at 90 °C for 5 min with continuous stirring. Then, the solution was cooled at room temperature with constant stirring and again heated up to 90 °C. At 90 °C, 5 ml of oleic acid was poured as a surfactant. The solution was cooled down slowly with continuous stirring until the temperature reached room temperature. A few drops of HNO₃ were added to attain a pH value of 7. The precipitate was cleaned with hot distilled water and acetone. Then, the sediment was dried at 60 °C for 3 h on a hot plate. The dried powder was annealed at 300 °C for 3 h in an electric furnace. All three samples were prepared under similar experimental conditions. The prepared powder samples were characterized using various techniques.

2.2 Characterization techniques

For microstructural and phase purity analysis, the XRD patterns were obtained employing the Panalytical X'Pert PRO diffractometer utilizing the Cu-K α line source ($\lambda \approx 1.5406 \text{ \AA}$). The diffractograms of intensity versus angle (2θ) were obtained at a step size of 0.02° in the range 20° to 70° . A superconducting quantum interference device (SQUID) (Quantum Design MPMS-3) was used for the magnetization measurements. The FC-ZFC data were collected at 500 Oe magnetic field between 4 and 300 K, while the magnetic moments versus magnetic field (M-H) curves were taken at 300 K. X-ray photoelectron spectroscopy (XPS) has been used to investigate the chemical stoichiometry of the surface. The sample's surfaces were cleaned with argon ion sputtering and the XPS data were collected using an Al K α X-ray line source in a vacuum $\sim 5 \times 10^{-10}$ Torr. The UV-Visible absorption spectra were used to explore the band gap of the prepared samples. The absorption spectra were measured at 300 K using the UV-visible spectrometer (Model: Lambda 900, Make: Perkin Elmer) with wavelengths varying from 200 to 800 nm. The photoluminescence (PL) spectra were used to analyze defect-related features. The PL spectra were taken at an excitation wavelength of 300 nm within the wavelength range of 360 nm to 550 nm at 300 K using the fluorescence spectrophotometer (Model: FL 8500, Make: Perkin Elmer).

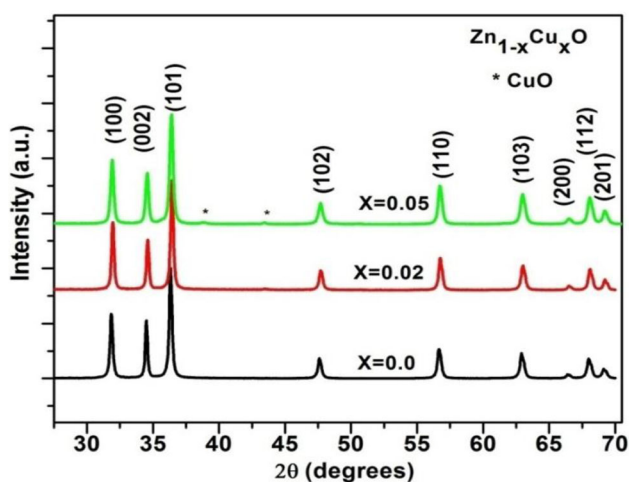


Fig. 1 XRD patterns for Cu-doped ZnO (Cu = 0%, 2% and 5%) nanoparticles

3 Results and discussion

3.1 XRD analysis

The XRD patterns of all the prepared Cu-doped ZnO nanoparticles (Cu = 0%, 2% and 5%) are displayed in Fig. 1. The patterns are consistent with the wurtzite crystal structure of ZnO (JCPDS Card No. 36-1451) [40]. All the reflection peaks were assigned Miller indices corresponding to the $P6_3mc$ space group with a hexagonal wurtzite structure. The atomic position for Zn is $(1/3, 2/3, 0)$ and for O it is $(1/3, 2/3, 0.3817)$ [26, 41]. The diffraction peaks in all the samples (Cu = 0%, 2% and 5%) correspond to the planes (100), (002), (101), (102), (110), (103), (200), (112) and (201) and were obtained at 31.8° , 34.5° , 36.3° , 47.6° , 56.6° , 62.9° , 66.4° , 68.0° and 69.1° , respectively [42]. It indicates that the Zn sites have been substituted with Cu ions without changing the ZnO crystal structure. It is because of the fact that the Cu^{2+} ions can easily penetrate the crystal lattice of ZnO due to their ionic radius (0.73 \AA) being closer to that of Zn^{2+} (0.74 \AA) [43]. The CuO peaks, quite small in intensity, were observed in the 5%Cu-doped ZnO nanocrystalline sample at 38.9° and 43.5° .

Figure 2 depicts the Rietveld-refined XRD patterns of the Cu-doped ZnO (Cu = 0%, 2% and 5%) nanocrystalline samples. The Chi-squared values (χ^2) for the nanocrystalline ZnO samples, the $\text{Zn}_{0.98}\text{Cu}_{0.02}\text{O}$ and the $\text{Zn}_{0.95}\text{Cu}_{0.05}\text{O}$, were calculated to be 3.46, 2.54 and 5.73, respectively. The refinement results appear to be quite reliable in view of the low χ^2 values [44]. Furthermore, significant broadening in the most intense peak (101) reflection, as depicted in Fig. 3, is a distinct indication of the nanocrystalline structure of the synthesized samples. The Scherrer formula given below was utilized to assess the average size of prepared Cu-doped ZnO nanocrystalline samples:

$$D = \frac{0.9\lambda}{\beta \cos \theta}$$

Here, D is the crystallite size, λ the wavelength of X-ray radiation, θ the diffraction angle and β is the full width at half maximum (FWHM) [45]. Crystallite sizes have been found in the range of 26 to 32 nm for all synthesized samples.

The Stokes–Wilson relationship was used to determine the microstrain (ϵ) created in nanocrystallites [43].

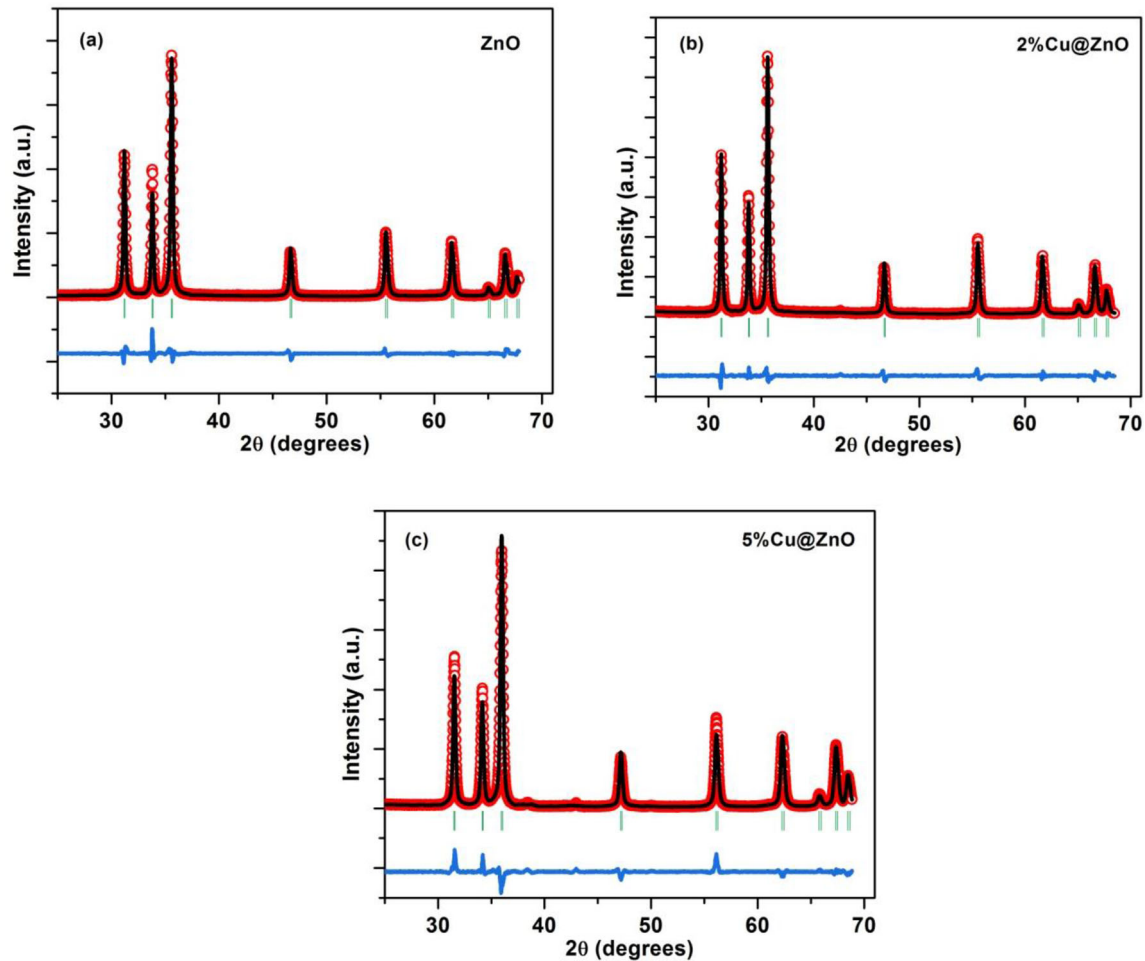


Fig. 2 Rietveld refined XRD patterns for: **a** pure ZnO, **b** the 2% Cu-doped ZnO and **c** the 5% Cu-doped ZnO nanoparticles. Observed data is shown by red dots and black solid line is the

calculated profile and the lower plot is the difference curve. Bragg peak positions are marked by vertical green lines (Color figure online)

$$\varepsilon = \frac{\beta}{4 \tan \theta}$$

Table 1 depicts the lattice parameters and c/a ratio for all the prepared samples, as well as the parameters of the most intense (101) peak as 2θ position, FWHM, crystal size D (nm), and microstrain.

The value of c/a was found to be 1.6 for all the samples, which indicates an ideally close-packed hexagonal structure [43]. The lattice parameters have been reduced slightly upon Cu doping into the ZnO lattice, confirming that the Cu is appropriately doped into the ZnO lattice structure. The strain caused by the number of defects formed with increasing Cu concentration is responsible for lowering the lattice parameters of the synthesized samples [45]. The peak position corresponding to (101) crystal plane shifts

upon Cu doping for the synthesized samples as depicted in Fig. 3. The observed shift in peak position towards the higher angles upon Cu doping is because of the substitution of the Zn^{2+} ions by the smaller sized Cu^{2+} ions, indicating a decrease in the lattice constants [46]. The reduced values of FWHM and the microstrain (as shown in Table 1) are liable for the increased crystallite size for 2% Cu-doped ZnO nanoparticles [47]. The decrease in size for 5% Cu-doped ZnO nanoparticles is because of the increase in microstrain [48].

Figure 4 shows the crystallite size and microstrain as a function of Cu concentration. Figure 4 shows that for the 2% Cu, the microstrain is reduced and the crystal size increased; on the contrary, for the 5% Cu-doped sample, the microstrain is increased, and the size is decreased.

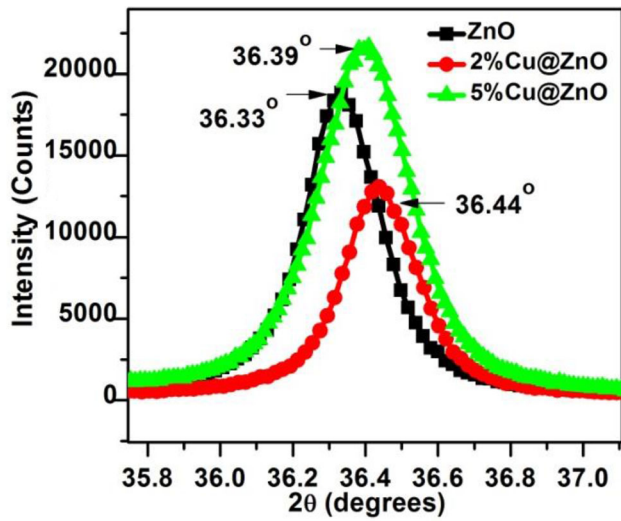


Fig. 3 The magnified view of the XRD patterns of the Cu-doped ZnO nanoparticles (Cu = 0%, 2%, 5%) between 35.8° and 37° of the (101) plane

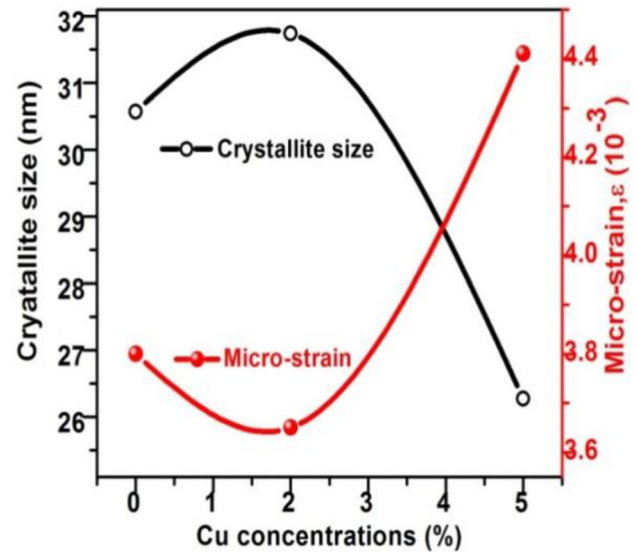


Fig. 4 The variation in crystallite size and microstrain with the Cu concentration (0%, 2% and 5%) for Cu-doped ZnO nanoparticles

The changes in oxygen occupancy in the Cu-doped ZnO samples were examined by Rietveld refinement analysis. The following equation is used to calculate changes in oxygen occupancy [49].

$$\Delta g_o = [g_o(\text{ZnO}) - g_o(\text{ZnCuO})]/g_o(\text{ZnO})$$

Here, g_o represents the oxygen site occupancy and Δg_o represents the difference in oxygen occupancy [49].

Figure 5 exhibits the changes of Δg_o with Cu concentration in percentage. The values of Δg_o for the 2% Cu and 5% Cu-doped ZnO samples have been obtained -0.0458 and -0.0281 , respectively. As Δg_o for the Cu-doped samples is found to be negative, which is a clear signature of increment in oxygen vacancy. Moreover, the higher negative value of Δg_o in the 2% Cu-doped sample compared to that in the 5% Cu-doped ZnO sample indicates more oxygen vacancy in the 2% Cu-doped sample. These results

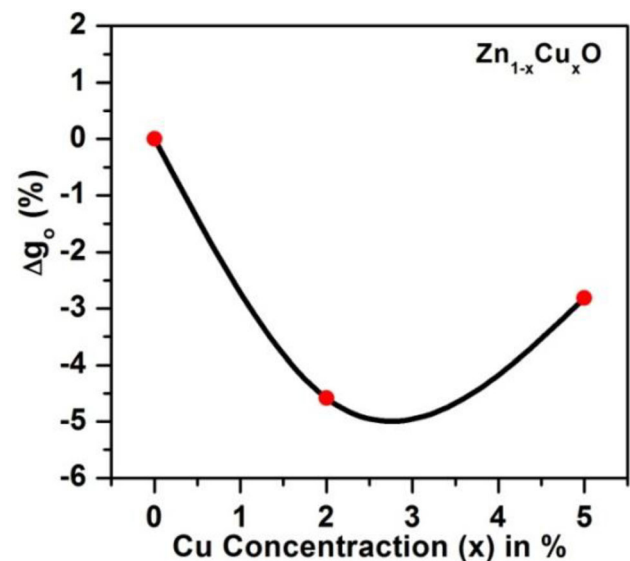


Fig. 5 The value of Δg_o versus the Cu concentration

Table 1 The values of lattice constants, c/a ratio; parameters for (101) peak; 2θ position, FWHM, crystal size D (nm) and Micro-strain for all the synthesized samples

Samples	Cu-doped ZnO Lattice parameters (Å)		c/a Ratio	2θ (degree)	FWHM β (degrees)	Crystal size D (nm)	Micro-strain ϵ (10^{-3})
	a=b	c					
0% Cu	3.3093	5.3022	1.6	36.3367	0.2857	31	3.80
2% Cu	3.3078	5.3005	1.6	36.4404	0.2752	32	3.65
5% Cu	3.2759	5.2492	1.6	36.3969	0.3325	26	4.41

show a fair agreement with our XPS results (to be discussed in detail later).

3.2 SEM analysis (microstructural studies)

The SEM micrographs have been used to analyze the impact of Cu doping on the surface morphology, size and shape of the grains or particles in the Cu-doped ZnO nanoparticles. Figure 6a–c depicts SEM images of the synthesized Cu-doped ZnO (Cu = 0%, 2% and 5%) nanoparticles. The surface morphology of the pure ZnO nanoparticles is depicted in Fig. 6a which exhibits the irregular grain size distribution and agglomerated spheroid-like particle structure. The morphology of the Cu-doped ZnO (Cu = 2% and 5%) nanoparticles is depicted in Fig. 6b and c. The formation of defect states causes slight changes in the size of particles, though there is no discernible change in the shape of the grain [48]. Most of the particles are found to have size between 20 and 60 nm, suggesting that dopant concentration may have also contributed to particle aggregation. As the dopant amount increases, the average particle size tends to change. Additionally, the diversity in morphology may be explained by the effect of Cu ions, which are used as doping agents, on the growth rate of ZnO nanoparticles [50]. The average particle size of the samples observed by SEM micrographs agrees well with those estimated from the XRD patterns.

3.3 X-ray photoelectron spectroscopy analysis

The XPS has been employed to explore the electronic and chemical states of the ZnO and Cu-doped ZnO nanoparticles, in terms of the valence state of the cations, the estimate of oxygen vacancies, etc. The carbon *C1s* peak (284.8 eV) reference has been used to calibrate all the binding energies (BE) of the XPS spectra. The XPS survey spectra (as depicted in Fig. 7) of all the prepared Cu-doped ZnO samples exhibit the Zn, Cu and O peaks, and no extra peaks are detected.

Figure 8 depicts the high-resolution XPS spectra of the Zn2*p* peak for the ZnO and the Cu-doped ZnO (Cu = 2% and 5%) nanoparticles.

For all the synthesized samples, i.e., the ZnO and the two Cu-doped ZnO nanocrystalline samples, the binding energies of the Zn2*p*_{3/2} and Zn2*p*_{1/2} peaks have been found to be at 1021.45 eV and 1044.51 eV,

respectively, with a shake-up structure at 1039.8 eV, as shown in Fig. 8. The characteristic Zn2*p* doublet peaks and the energy positions corresponds to the divalent oxidation state of Zn, i.e., Zn²⁺, in all the samples [34, 51, 52]. The energy separation between Zn2*p*_{3/2} and Zn2*p*_{1/2} peaks is 23 eV which is consistent with the previously reported values [53]. With Cu doping, the binding energies of Zn2*p* peaks abide stationary, showing that the doping of Cu into ZnO nanoparticles does not influence the chemical environment of Zn²⁺.

The asymmetric shape of the O1*s* XPS high-resolution spectra for all the prepared samples (as exhibited in Fig. 9a) reveals the existence of multi-component oxygen species at the surface of the samples [54].

The O1*s* XPS spectra have been fitted with three Gaussian peaks for all the prepared nanocrystalline samples (as depicted in Fig. 9b–d). The three deconvoluted O1*s* peaks are found to be located at the binding energies of 530.12 eV, 531.45 eV and 532.58 eV in the ZnO nanoparticles (as displayed in Fig. 9b). The assignment of the peaks is as follows: the lower binding energy peak is due to lattice oxygen in the hexagonal ZnO wurtzite structure, whereas the middle peak is related to oxygen vacancies in the ZnO matrix [27]. The higher binding energy peak is because of adsorbed oxygen molecules (chemisorbed oxygen, OH⁻ and adsorbed H₂O) on nanocrystals' surfaces [27, 51]. The deconvoluted O1*s* peaks in the Zn_{0.98}Cu_{0.02}O sample are found at 530.03 eV, 531.05 eV, and 532.58 eV binding energy positions and in the Zn_{0.95}Cu_{0.05}O sample; these are found at 530.01 eV, 531.13 eV and 532.45 eV, respectively (shown in Fig. 9c and d). An additional low intensity peak is observed in both the Cu-doped samples at the lower side of the first peak. The binding energy position is at 528.88 eV in the Zn_{0.98}Cu_{0.02}O sample and 528.57 eV in the Zn_{0.95}Cu_{0.05}O nanocrystalline sample. This peak represents the CuO lattice in the samples [51]. Notably, the lattice oxygen and oxygen vacancies peaks in the O1*s* spectra have shifted slightly towards the lower binding energy in the Cu-doped ZnO samples as compared to the pure ZnO (as shown in Table-2). This shift can be attributed to zinc interstitials and/or increased density of oxygen vacancies at the ZnO surface. Comparing the peak area ratios, we see that the 2% Cu-doped sample has 32.29% lattice oxide, which is less than the values 57.33% for the pure ZnO

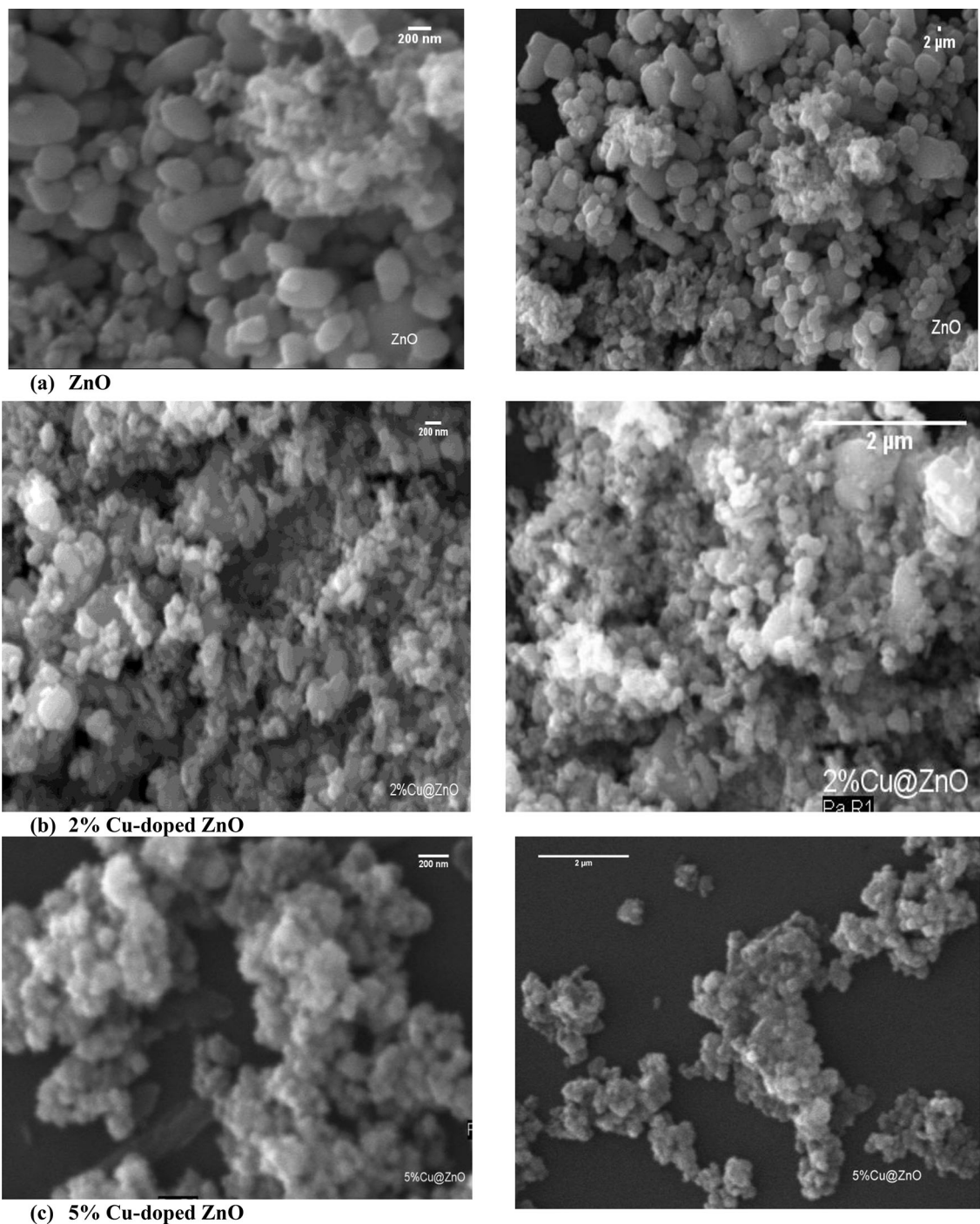


Fig. 6 SEM micrographs **a** for the ZnO, **b** for the 2% Cu and **c** for the 5% Cu-doped ZnO nanoparticles

and 39.02% for that in the 5% Cu-doped ZnO. Table 2 shows that the oxygen vacancies in 2% Cu-doped sample are 38.69%. This value is higher than the oxygen vacancies in the pure ZnO (31.53%) and that in the $Zn_{0.95}Cu_{0.05}O$ nanocrystalline sample (33.29%). Thus, we can say that the 2% Cu-doped sample has the lowest concentration of metal-oxide bonds and

the highest percentage of oxygen vacancies. Similar observations have been reported in the literature in the Cu-doped samples [34, 55].

Figure 10a, b display the high-resolution XPS spectra of the Cu2p peaks for the $Zn_{0.98}Cu_{0.02}O$ sample and the $Zn_{0.95}Cu_{0.05}O$ sample. The Cu2p spectra consist of two broad peaks $2p_{3/2}$ and $2p_{1/2}$

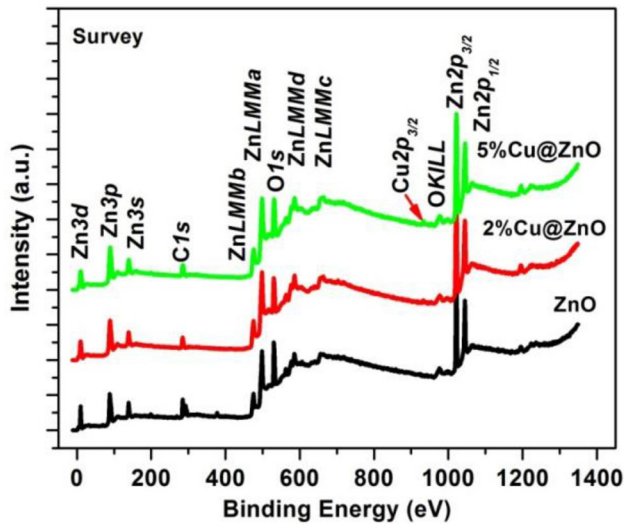


Fig. 7 XPS survey spectra for ZnO and Cu-doped ZnO (Cu = 2% and 5%) nanoparticles

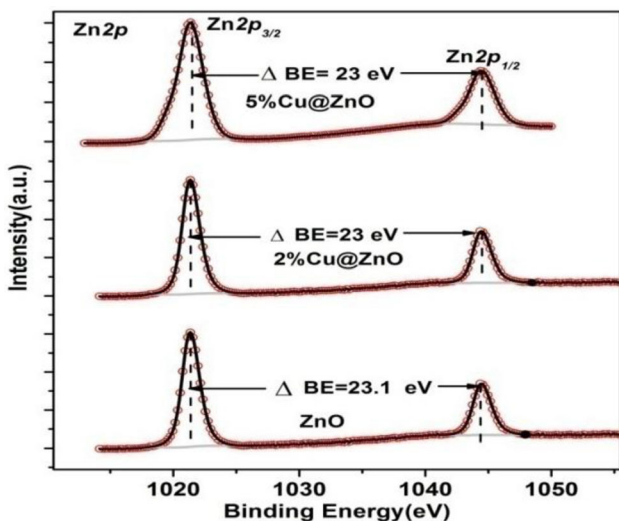


Fig. 8 XPS spectra for Zn2p peaks of the pure and Cu-doped ZnO (Cu = 2% and 5%) nanoparticles

produced because of the spin–orbit splitting of the Cu2p states. In the Zn_{0.98}Cu_{0.02}O sample, the Cu2p_{3/2} and Cu2p_{1/2} peaks are detected at 932.77 eV and 952.52 eV, respectively, whereas in the Zn_{0.95}Cu_{0.05}O sample, these were found to be located at energy positions 932.69 eV and 952.43 eV, respectively.

The Zn_{0.98}Cu_{0.02}O and Zn_{0.95}Cu_{0.05}O samples have an asymmetrical peak of Cu2p_{3/2} and have fitted two Gaussian curves, as depicted in Fig. 10a, b. The binding energy separation between the spin–orbit doublet splitting of Cu2p_{3/2} and Cu2p_{1/2} peaks is ~20 eV [42]. In addition, the satellite peaks are

observed at 941.83 eV for the Zn_{0.98}Cu_{0.02}O sample and at 941.45 eV for the Zn_{0.95}Cu_{0.05}O sample. The divalent state of Cu ions in the ZnO matrix is responsible for these features [56]. Additionally, the monovalent copper (Cu¹⁺) peaks Cu2p_{3/2} and -Cu2p_{1/2} have also been observed at 931.6 eV and 951.7 eV binding energies, respectively, with slightly narrower signal peak widths in the fitted Cu2p spectra. Thus, we can say that the Cu2p_{3/2} peak is the mixture of the two peaks corresponding to the Cu²⁺ and the Cu¹⁺ states and is present in all Cu-doped ZnO samples, consistent with the previous Cu-doped ZnO studies [5, 57]. In fact, the divalent copper ion (Cu²⁺) signals get shifted towards the higher binding energy side by ~1.6 eV, as compared to the Cu¹⁺ ions [26]. The observed co-existence of some Cu¹⁺ ions (lesser valence state than bivalence state) in the Cu-doped samples further supports the creation of more oxygen vacancies from the charge neutrality consideration in the lattice. Table 2 displays the Zn2p, Cu2p and O1s peaks fitting parameters, including peak position and O vacancy/O lattice ratio.

The area ratio of the oxygen vacancy peak and the lattice oxygen peak (V_o/L_o) is found to get enhanced upon Cu doping, as shown in Table 2, indicating the remarkable evolution of oxygen vacancies with Cu doping [34]. The value of the ratio (V_o/L_o) is found to be the maximum in the 2% Cu-doped sample (~1.19) as compared to the 5% Cu-doped sample (~0.85) and the pure ZnO (~0.54) nanoparticles. Thus, the 2% Cu-doped ZnO sample exhibits maximum oxygen vacancies.

3.4 Optical properties

3.4.1 Study of ultraviolet–visible absorption spectra and the energy gap

The UV–visible absorption spectra for the Cu-doped ZnO nanoparticles (Cu = 0%, 2% and 5%), recorded between 300 and 800 nm wavelengths, exhibit a sharp peak in the UV region, as shown in Fig. 11. The absorption bands and intensity are influenced by various factors including the energy gap, the oxygen vacancies and the defect sites [58]. The absorption edges of the pure ZnO, Zn_{0.98}Cu_{0.02}O and Zn_{0.95}Cu_{0.05}O nanocrystalline samples have been detected at 378 nm, 380 nm and 379 nm, respectively. The crystallite size impact is responsible for the shift of the absorption edge [59]. The absorption of the 2%

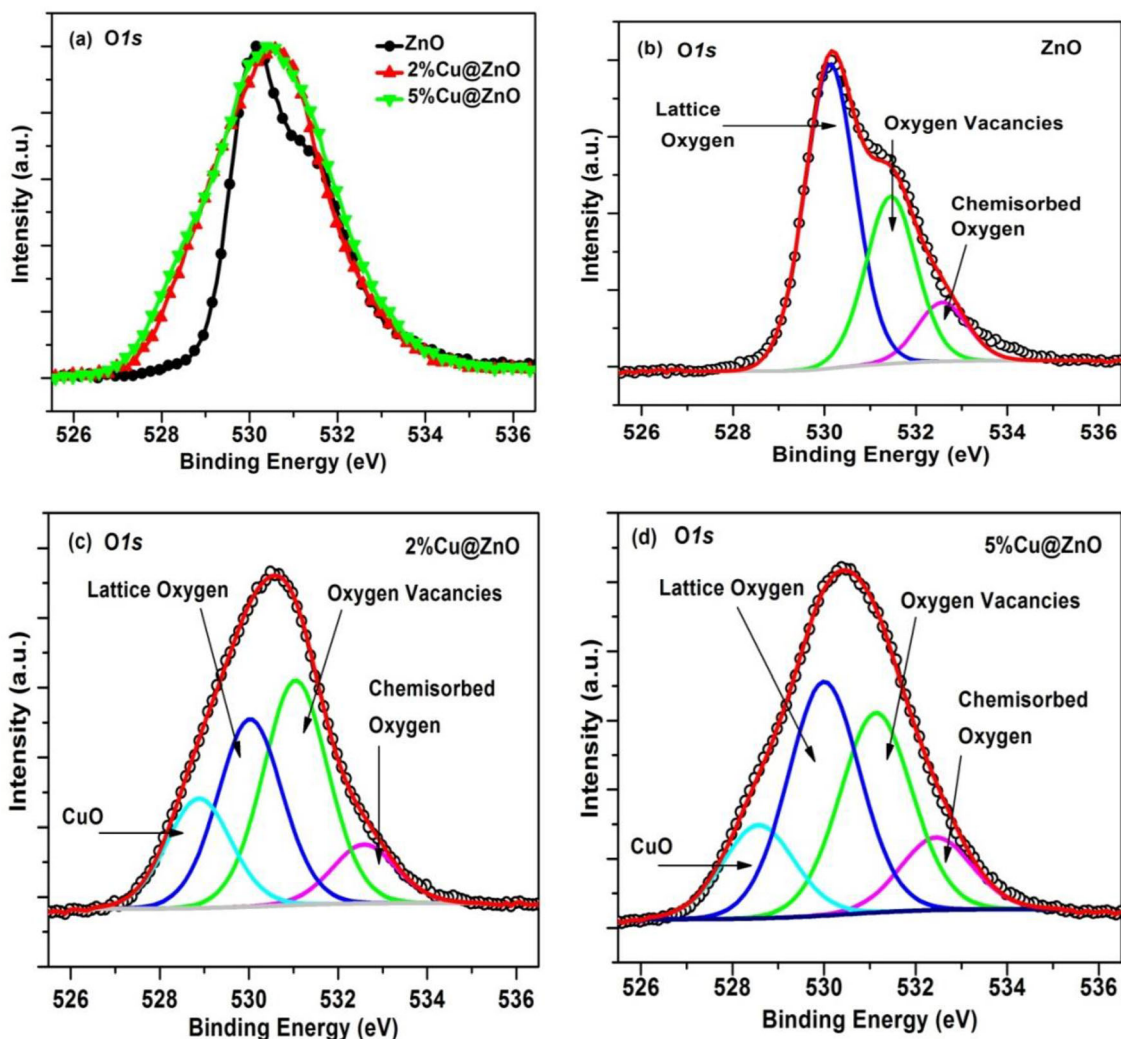


Fig. 9 a Asymmetric O1s XPS spectra for all the prepared samples. The O1s core level XPS spectra have been fitted with three Gaussian peaks. b for pure ZnO c for the 2% Cu-doped ZnO and d for the 5% Cu-doped ZnO nanoparticles

Cu-doped sample has been reduced considerably as compared to the other two samples. Therefore, the spectrum of the $\text{Zn}_{0.98}\text{Cu}_{0.02}\text{O}$ sample is depicted separately in the inset. A decrease in the intensity of the $\text{Zn}_{0.98}\text{Cu}_{0.02}\text{O}$ sample is attributed to more defects in it [60]. The absorption for the $\text{Zn}_{0.95}\text{Cu}_{0.05}\text{O}$ nanocrystalline sample has increased [61] because the charge carrier density decreases on further Cu doping due to the generation of secondary phase CuO. The Tauc's equation, which depicts a relationship between the absorption coefficient and incident photon energy of the semiconductors, has been used to determine the optical band gap of the Cu-doped ZnO nanocrystalline samples (Cu = 0%, 2%, and 5%). The Tauc's equation is [62]:

$$\alpha h\nu = A(h\nu - E_g)^n$$

Here, A is a constant; the exponent n is 1/2 for the direct band gap, E_g is the band gap of the semiconductor material, α is the absorption coefficient and h is the plank's constant. The E_g of the Cu-doped ZnO samples has been calculated by plotting $(\alpha h\nu)^2$ versus $h\nu$, shown in Fig. 12. Here $h\nu$ is photon energy in eV.

The value of E_g is calculated by extrapolating the linear portion of the $(\alpha h\nu)^2$ to intersect with the $h\nu$ portion. The value of band gap energies is found to decrease upon Cu doping as compared to the pure ZnO nanoparticles. The values of E_g obtained for the undoped ZnO sample, the $\text{Zn}_{0.98}\text{Cu}_{0.02}\text{O}$ sample and the $\text{Zn}_{0.95}\text{Cu}_{0.05}\text{O}$ sample are 3.15 eV, 2.96 eV, and

Table 2 The XPS elemental investigation and stoichiometry of the Cu-doped ZnO nanocrystalline (Cu = 0%, 2% and 5%) samples

Sample Cu-doped ZnO	B.E. of Zn2p peaks (eV)	B.E. of Cu2p _{3/2} peaks (eV)		B.E. of O1s peaks (eV)			Ratio of V _o /L _o
		Cu ²⁺	Cu ¹⁺	Position	O-type	% Area	
0% Cu	1021.40 2p _{3/2}			530.12	Lattice Oxygen	57.33	0.54
	1044.51 2p _{1/2}			531.45	Vo	31.53	
				532.58	–OH	11.14	
2% Cu	1021.45 2p _{3/2}	933.13	931.62	528.88	CuO	18.86	1.19
	1044.51 2p _{1/2}			530.03		32.29	
				531.05		38.69	
5% Cu	1021.34 2p _{3/2}	933.05	931.74	528.57	CuO	15.54	0.85
	1044.41 2p _{1/2}			530.01		39.02	
				531.13		33.29	
				532.45		12.14	

*V_O Oxygen Vacancy, – OH Chemisorbed Oxygen

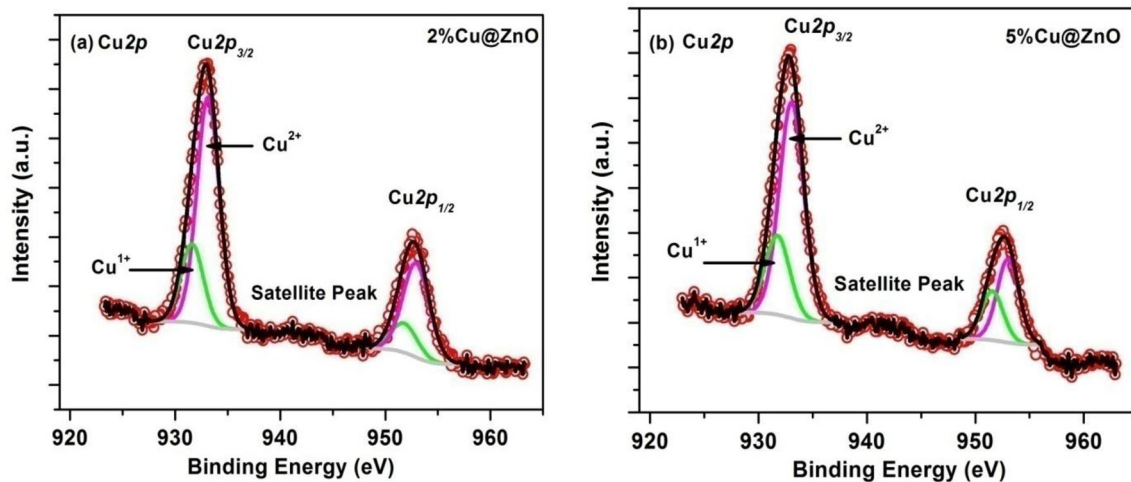


Fig. 10 The Cu2p_{3/2} peak of the XPS spectra fitted with two Gaussian peaks for the **a** 2% Cu-doped ZnO nanoparticles and **b** 5% Cu-doped ZnO nanoparticles

3.0 eV, respectively. Further, the redshift ΔE obtained for the Zn_{0.98}Cu_{0.02}O sample is ≈ 0.19 eV and for the Zn_{0.95}Cu_{0.05}O sample, the redshift is ≈ 0.15 eV.

Bhardwaj et al. [63] found similar results, and they ascribed the lowering of the band gap to the significant defect levels observed in the Cu-doped ZnO nanocrystalline samples. The observed redshift in E_g is ascribed to oxygen-related defects and the decrease in charge carrier density. According to Noipa et al. [57], the sp-d spin-exchange interactions between the band electrons and the localized d electrons of the Cu²⁺ ions substituted in place of the Zn ions are

responsible for the redshift. Figure 13 displays the relationship between crystallite size and the energy gap versus the Cu concentration (Cu = 0%, 2% and 5%).

The density of defects due to impurity atoms and variations in the size and structure of the material often alters the energy gap [64]. The crystallite size and the energy band gap are often inversely proportional to each other [48, 65]. For the 2% Cu-doped sample, the E_g has reduced and the size increased, following the above relation [65]. The 2% Cu doping

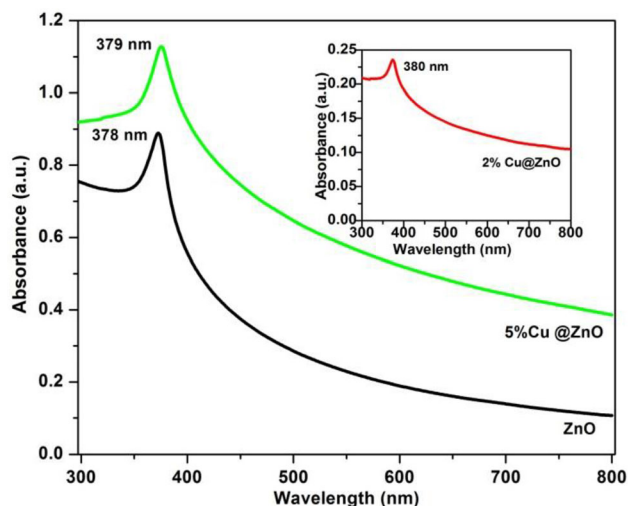


Fig. 11 The UV–Visible absorption spectra for wavelength range 300 to 800 nm for the pure ZnO and the 5% Cu-doped ZnO nanoparticles. The spectrum for the 2% Cu-doped ZnO nanoparticles is exhibited in the inset

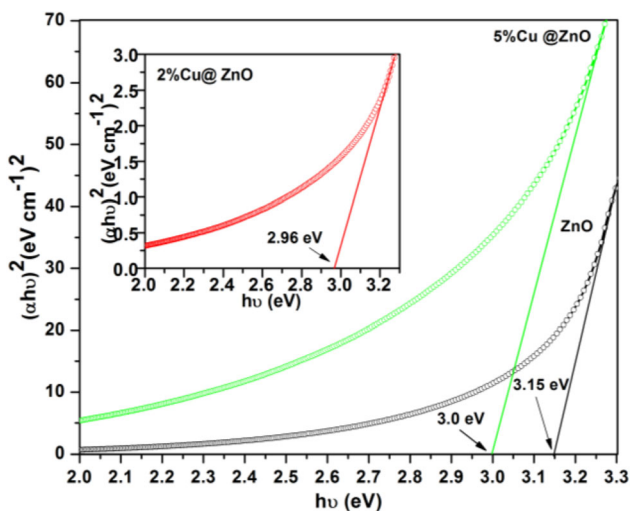


Fig. 12 Tauc's plot for the samples of Cu-doped ZnO nanoparticles (Cu = 0% and 5%) with an inset for the 2% Cu-doped ZnO nanoparticles sample

into the ZnO lattice is found to generate more defects, which is responsible for a reduction in the E_g .

3.4.2 Photoluminescence (PL) analysis

The PL spectroscopy has been utilized to analyze the structural defects and crystalline structure quality of the Cu-doped ZnO nanoparticles. The spectra have been recorded using 300 nm excitation wavelength at room temperature. The PL spectra for all the samples are exhibited in Fig. 14a.

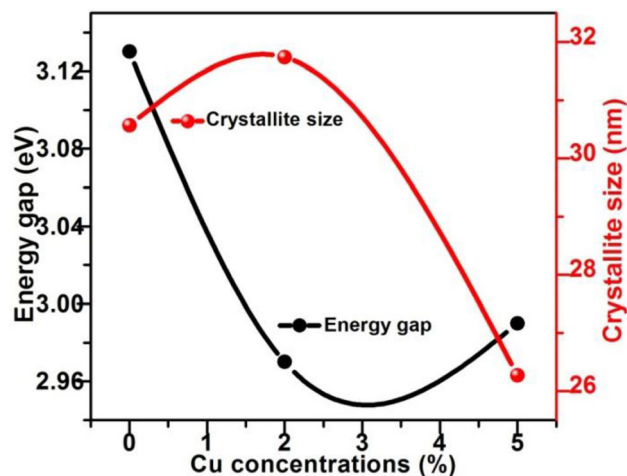


Fig. 13 The crystallite size and the energy gap fluctuations of the synthesized samples as a function of Cu doping levels

It is observed that all the prepared samples have the following emission bands: (i) Ultra-violet (UV) emission region, (ii) Violet emission region, (iii) Blue emission region and (iv) Green emission region [61]; all these regions are shown in the Fig. 14a. Then the PL spectra of all the Cu-doped ZnO (0%, 2% and 5%) nanoparticle samples were deconvoluted using Gaussian fitting, revealing seven peaks, as shown in the Fig. 14a–c. The UV emission peak corresponding to near-band emission (NBE) has been detected at 386 nm for ZnO, 380 nm for $Zn_{0.98}Cu_{0.02}O$ and 387 nm for $Zn_{0.95}Cu_{0.05}O$. The UV (NBE) peak could be caused by free excitons recombination [66]. In the violet region, the peak was found at 404 nm for ZnO, 394 nm for the 2% Cu-doped sample and 407 nm for the 5% Cu-doped sample which is known to be generated by the transition between the zinc interstitials (Zn_i) and the valance band of ZnO [67, 68]. The other violet emission peaks obtained at 426 nm and 448 nm for ZnO, at 416 nm and 440 nm for $Zn_{0.98}Cu_{0.02}O$ and at 427 nm and 449 nm for $Zn_{0.95}Cu_{0.05}O$ are ascribed to the transition from the bottom level of the conduction band (E_c) to zinc vacancy (Zn_v) and the transition of electrons from the zinc interstitial (Zn_i) state to the top of the valance band (E_v) [69]. The observed shift in the violet region peaks with Cu doping re-confirms that Zn is replaced by Cu ions in the ZnO structure, which is attributed to Zn_i vacancies [63]. The deep-level or defect luminescence produced by the oxygen vacancies is the origin of the blue emission peak at 448 nm in ZnO, 440 nm in the 2% Cu-doped sample, and at 449 nm in the 5% Cu-

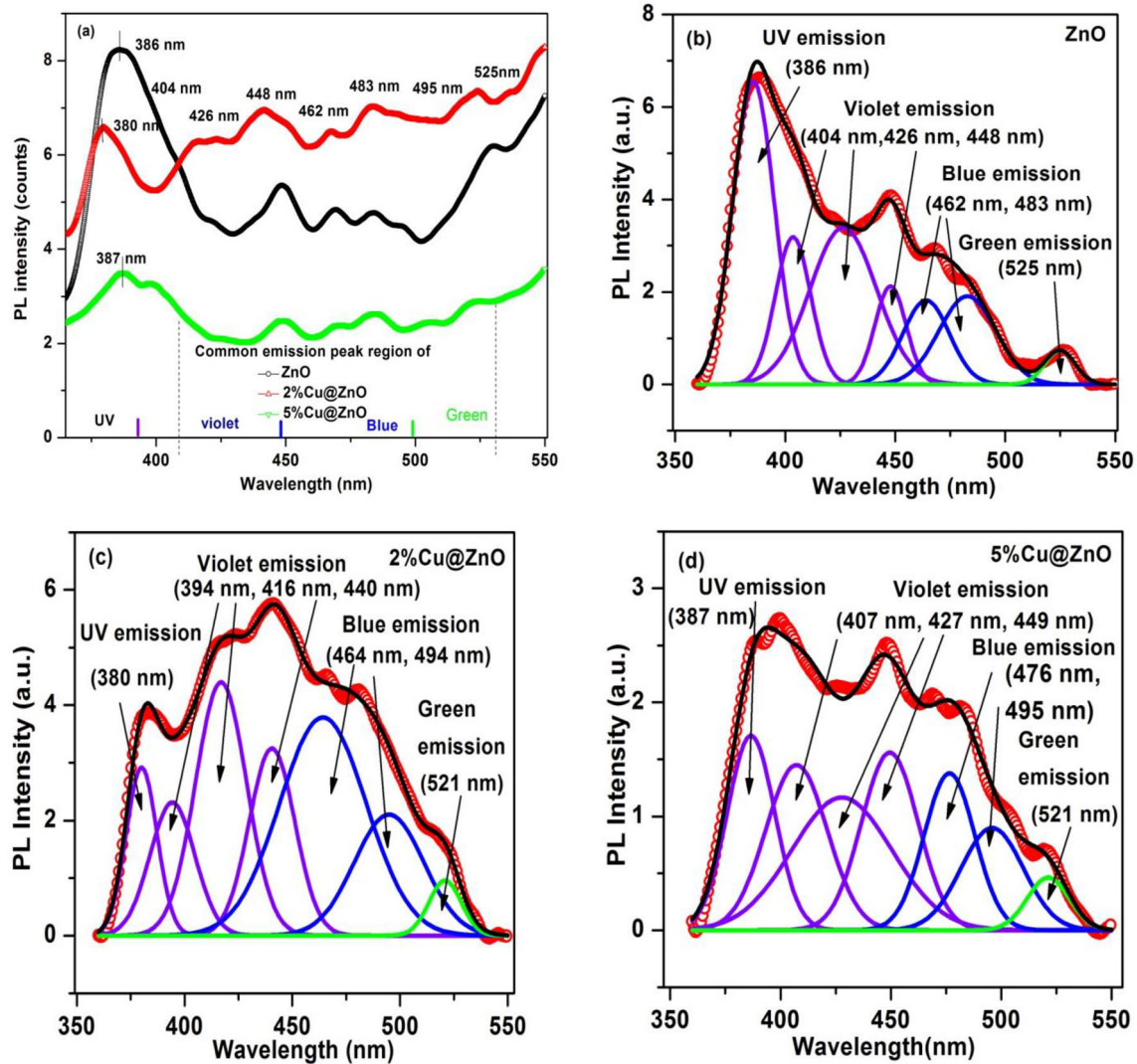


Fig.14 a The PL spectra of the ZnO and the Cu-doped ZnO nanoparticles at room temperature with different Cu concentrations and the Gaussian fitted PL spectra for b pure ZnO c for the 2% Cu-doped ZnO and d for the 5% Cu-doped ZnO nanoparticles

doped sample [70]. The peak in the blue radiation region has been found at 462 nm for ZnO, at 464 nm for the 2% Cu-doped sample and at 476 nm for the 5% Cu-doped sample because of deep-level emission [71]. The peak at 483 nm in ZnO is caused by the transition from the shallow donor level of the Zn interstitial to the valance band [63, 67]. Two peaks were detected in the green emission, the first at 494 nm and the second at 525 nm, for the 2% Cu-doped sample. For the 5% Cu-doped sample, these peaks are observed at 494 nm and 525 nm, respectively. These peaks are attributed to the presence of oxygen vacancies on the ZnO surface [64, 72]. The green emission at 525 nm for ZnO and 521 nm for the Cu-doped samples is because of the transition

between the weakly captured electron and the strongly captured hole in the singly ionized oxygen vacancies (V_o^+) [73]. Therefore, with increasing Cu concentration in the ZnO nanoparticles, the corresponding increase in the intensity of green emission and decrease in the UV emission re-confirms the presence of defect-related states [61]. Figure 15 depicts the change in the intensity of UV emission and the intensity ratio between the green and the UV emission as a function of Cu concentration. The Cu doping reduces the UV emission intensity.

Notably, the intensity ratio of the green and the UV emission (I_G/I_{UV}) is found to be more for the 2% Cu-doped sample than for the 5% Cu-doped sample and the pure ZnO. The maximum value of the I_G/I_{UV}

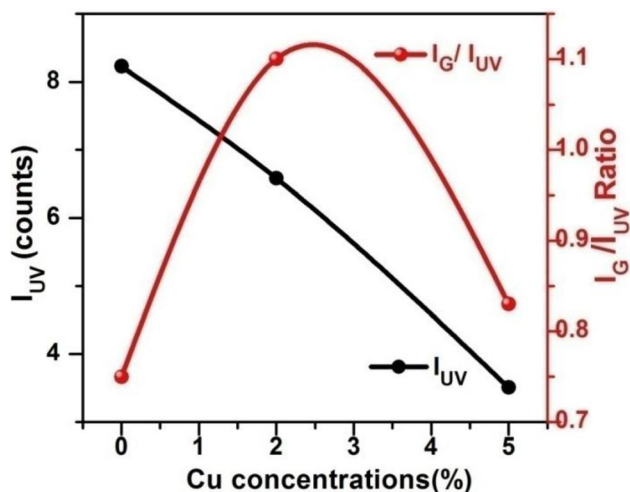


Fig. 15 The variations in the intensity of UV emission and the intensity ratio of the green and UV emissions with Cu concentration

ratio in the $\text{Zn}_{0.98}\text{Cu}_{0.02}\text{O}$ sample is due to presence of maximum oxygen vacancies in it [71]. These findings show a fair agreement with the XRD and the XPS results.

3.5 Magnetic evaluation

The magnetic characterization in the range of the field of 2 Tesla at 300 K and also the temperature variation of their magnetization was carried out for the Cu-doped ZnO nanoparticles. The M-H curve for the undoped ZnO nanocrystalline sample exhibits a weak ferromagnetic ordering at 300 K (shown in Fig. 16). However, the M-H curve's shape suggests

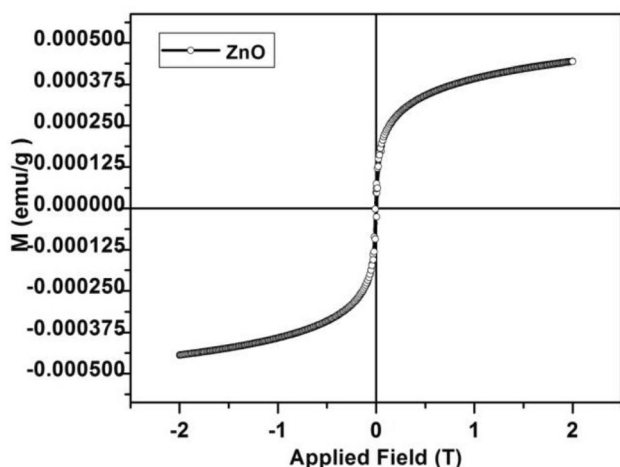


Fig. 16 Field variation with magnetization studied at 300 K for the undoped nanocrystalline ZnO

some paramagnetic contribution in the sample; therefore, the paramagnetic contribution was subtracted from the curve. Figure 17 displays the M-H curve for ZnO after deducting the paramagnetic contribution. The saturation magnetization comes out to be 3.71×10^{-4} emu/gm for the pure ZnO nanocrystalline sample.

This type of ferromagnetism in non-magnetic undoped oxide systems initially appeared unrealistic; however, the frequent finding in systems such as ZnO, HfO_2 , and MgO has unlocked new routes in magnetism research. Since these oxides have d-/f-orbitals either completely filled or empty, the intrinsic magnetism displayed by these undoped oxides without d-orbital electrons is known as d^0 ferromagnetism [74]. This magnetism is considered to be originated because of the polarization induced by p-orbitals. This magnetic polarization occurs because of the vacancies and the excitation of trapped spin in the triplet state. The magnetic properties of these oxides are influenced by the existence of oxygen vacancies at the surface and subsurface. Figure 18 displays the M-H curves measured at 300 K for the nanocrystalline $\text{Zn}_{0.98}\text{Cu}_{0.02}\text{O}$ sample and the $\text{Zn}_{0.95}\text{Cu}_{0.05}\text{O}$ sample.

The M-H curves exhibit giant ferromagnetic hysteresis loops for both the nanocrystalline samples $\text{Zn}_{0.98}\text{Cu}_{0.02}\text{O}$ and $\text{Zn}_{0.95}\text{Cu}_{0.05}\text{O}$, indicating that they show huge ferromagnetism at room temperature. The values of retentivity and saturation magnetization for the nanocrystalline sample $\text{Zn}_{0.95}\text{Cu}_{0.05}\text{O}$ (0.63×10^{-3} emu/gm and 4.61×10^{-3} emu/gm, respectively) fall

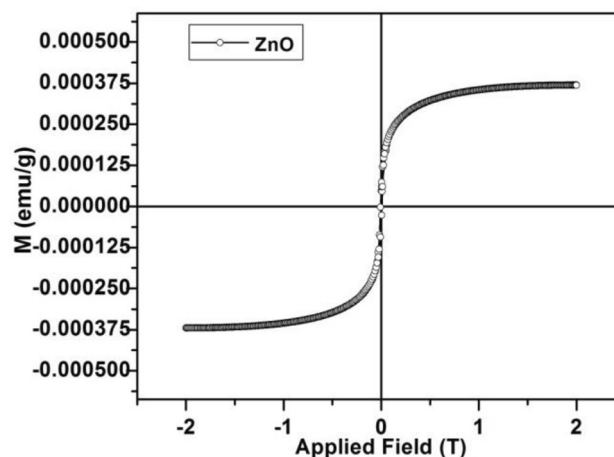


Fig. 17 Field variation with magnetization studied at 300 K for the nano-crystalline ZnO, only ferromagnetic contribution to the magnetism

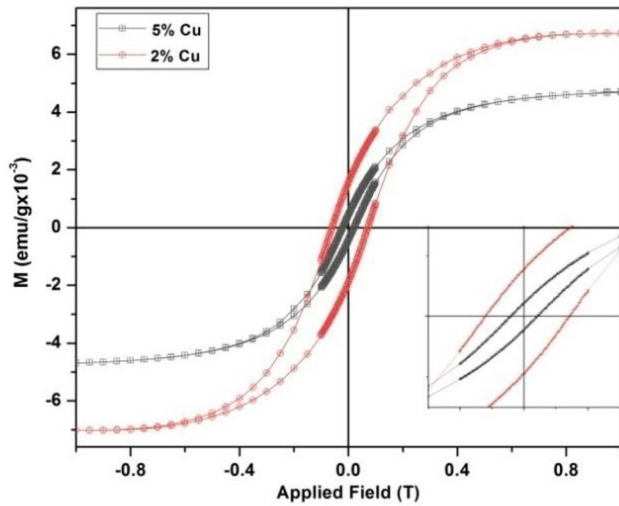


Fig. 18 The field variation of magnetization studied at 300 K for Cu-doped ZnO (Cu = 2% and 5%) nanocrystalline samples. The inset shows a magnified view of the low fields

remarkably compared to those for the sample $Zn_{0.98}Cu_{0.02}O$ (1.76×10^{-3} emu/gm and 6.73×10^{-3} emu/gm, respectively). Figure 19 depicts the temperature dependence of the magnetization for the sample $Zn_{0.98}Cu_{0.02}O$ under the zero field-cooled (ZFC) and field-cooled (FC) situations, measured at 500 Oe field.

The magnetic irreversibility behavior between ZFC and FC M-T data is notable. The divergence starts from 150 K and there is a continuous increase in it on lowering the temperature. The magnetic irreversibility/divergence between the ZFC and FC M-T curves

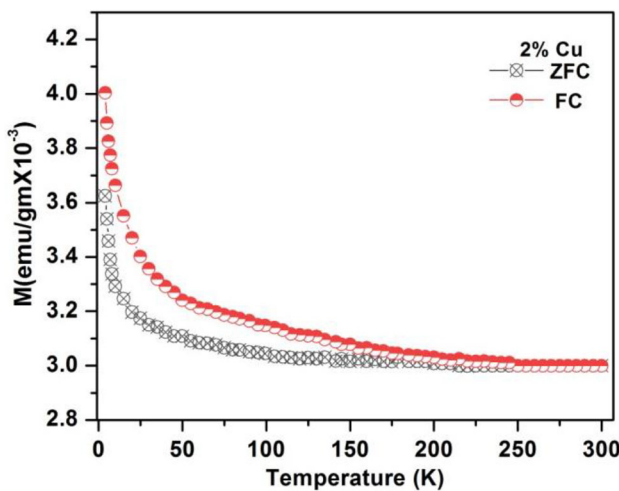


Fig. 19 The temperature variation of magnetization for the $Zn_{0.98}Cu_{0.02}O$ nanocrystalline sample measured at an applied field of 500 Oe

(as depicted in Fig. 19) may be attributed to the ferromagnetic ordering of the samples [75].

3.5.1 Discussion

The observed magnetization in the prepared Cu-doped ZnO (Cu = 0%, 2% and 5%) nanocrystalline samples displays a direct correlation with the oxygen vacancies. Let's remember the oxygen vacancies data we obtained from our XPS findings. The density of oxygen vacancies was observed to be suppressed in the $Zn_{0.95}Cu_{0.05}O$ sample considerably as compared to that in the $Zn_{0.98}Cu_{0.02}O$ nanocrystalline sample. The observed magnetization in them exhibits a similar trend. In case of the $Zn_{0.95}Cu_{0.05}O$ sample, the value of saturation magnetization is suppressed considerably compared to the $Zn_{0.98}Cu_{0.02}O$ sample. Thus, we can state that the conduct of magnetism displayed by the Cu-doped ZnO nanocrystalline samples appears to correlate with the oxygen vacancies that evolved in them. The mechanism of origin of ferromagnetism in these DMS systems has been a mystery, despite a lot of efforts made. We briefly discuss below the possible cause of the origin of ferromagnetism. According to most of the theoretical models, ferromagnetism strongly depends on creating and distributing oxygen vacancies in the Cu-doped ZnO lattice [76, 77]. According to Coey et al. [76], oxygen vacancies induce ferromagnetic coupling via an indirect exchange mechanism. They suggested the existence of exchange interaction between the carriers caught by O vacancies and the doped ions in the framework of the bound magnetic polaron (BMP) model [76]. The model states that the spin of localized defects (O vacancies) aligns with those of the nearby dopant ions, creating an influential magnetic field and activating ferromagnetic interactions in them. Although the different mechanisms by which various DMS systems produce ferromagnetism, they all have the same key feature that oxygen vacancies play a crucial role in ferromagnetism. Based on our findings and the above theoretical viewpoint, we are of the strong view that the observed ferromagnetism is caused by the exchange interactions between the Cu^{2+} ions and the oxygen vacancies [78–80].

In the recent past, the TM-doped ZnO system has been studied intensively. We present below a few relevant reports for comparison with our findings. Bhardwaj et al. [63] reported RTFM in the Cu-doped ZnO nanostructures. Their UV–vis results showed a reduction in the band gap upon Cu doping and the

PL findings indicated the occurrence of oxygen vacancies in them. They explained that intrinsic exchange interactions arising from oxygen vacancy-assisted bound magnetic polarons (BMPs) are responsible for RTFM in the Cu-doped ZnO nanostructures. Zhu et al. [5] reported RTFM in the Cu-doped ZnO samples prepared via hydrothermal process in the pulsed magnetic field. The creation of oxygen vacancy density up on Cu doping was suggested to be crucial for the origin of ferromagnetism. Noipa et al. [57] prepared the Cu-doped ZnO nanorods via the direct thermal decomposition process. Their UV-visible spectroscopy and the PL results exhibited the reduction in the band gap with increasing Cu amount and the creation of oxygen vacancies re-confirmed by the XPS. Their magnetic measurements revealed that ZnO is diamagnetic and Cu-doped ZnO samples exhibit RTFM properties. The 3.55% Cu-doped ZnO sample showed a higher density of oxygen vacancies and magnetization. Liu et al. [81] prepared Cu-doped ZnO nanoparticles using a solution route and annealed them in O₂, Ar and N₂, respectively. They suggested that the singly ionized oxygen vacancies play an essential role in the origin of ferromagnetism in the Cu-doped ZnO. Asih et al. [31] reported remarkable ferromagnetism in the Cu-doped ZnO nanoparticles thin films and claimed it to be due to the interaction with the spins of Cu3d⁹ through the oxygen vacancies and the Cu3d⁹ ligand holes. Ma et al. [82] reported a reduction in the band gap of Cu-doped ZnO samples with increasing Cu percentage. They claimed it to be due to the shift of the conduction band downwards by the introduction of Cu. Hadia et al. [83] reported similar findings on the Cu-doped ZnO nanowires. Hou et al. [84] studied Zn_{1-x}Cu_xO thin films, which exhibited RTFM and the moment per Cu ion was reported to decrease with increasing Cu. Chen et al. [85] studied Cu-doped ZnO nano-fibers and reported that Cu doping leads to a long-range FM ordering that was ascribed to the inducement of oxygen vacancies in them. Wang et al. [27] explored the origin of magnetism in Cu-doped ZnO nanocrystals. At 0.25 at.% of Cu, the saturated magnetization reached the maximum and then reduced with increasing Cu percentage. Thus, we can say that the main findings in our work, i.e., (i) the observed huge RTFM in the ZnO nanoparticles upon Cu doping, (ii) the reduction in magnetization upon Cu doping beyond 2% and (iii) the reduction in the band gap upon Cu doping, show a fair agreement

with the above reports. However, on the other hand, our results show a disagreement with those of Vachhani et al. [86], who studied the Cu-doped ZnO system with the Cu content varying from 2 to 10 at%. Their samples were found to retain paramagnetic character with no ferromagnetic ordering and also their results revealed evidence of antiferromagnetic interaction between the magnetic moments. Similar reports are from Qing-Yu et al. [87] on the 2% Cu-doped ZnO nanoparticles, who claimed that the sample retains paramagnetic character down to 5 K. Also, there are interesting reports from Wang et al. [88], who investigated the Cu-doped ZnO both in bulk and nanocluster and claimed that the magnetic phase has a transition from FM phase to AFM phase as the size for the doping system decreases from bulk to nanocluster.

4 Conclusions

Cu-doped ZnO nanoparticles have been prepared via the co-precipitation method and analyzed using various techniques such as XRD, SEM, XPS, PL, UV spectroscopy and SQUID measurements. All the synthesized nanoparticles exhibit the hexagonal wurtzite structure with a spheroid-like particle structure and the Cu²⁺ ions are substituted into the Zn sites. The pure ZnO and the Cu-doped ZnO nanoparticles display room-temperature ferromagnetism. The XRD and XPS analysis shows that the Cu doping into the ZnO lattice creates remarkable oxygen vacancies (V_o). The Zn_{0.98}Cu_{0.02}O nanocrystalline sample exhibit the maximum values of V_os and saturation magnetization. The density of oxygen vacancies (V_o) and magnetization decrease with an increase in the Cu concentration. The UV spectroscopy results show the reduction in the band gap on Cu doping. The band gap is reduced significantly in the Zn_{0.98}Cu_{0.02}O sample than that in the pure ZnO and Zn_{0.95}Cu_{0.05}O. The induced magnetization exhibits a direct relationship with the V_o. The PL spectra results show the maximum number of defects and V_os in the Zn_{0.98}Cu_{0.02}O nanocrystalline sample, as evidenced by the enhanced intensity ratio of the green and ultraviolet emission (I_G/I_{UV}). The PL and XPS results show a fair parallelism with each other regarding the induced defects i.e., the oxygen vacancies. The Cu-doped ZnO nanoparticles, which already contain essential features, become even more

of a prospective system for spintronic devices as room-temperature ferromagnetism is induced in them. The main advantages of spintronic devices include their small size, outstanding luminous efficiency, environmentally friendly composition, long persistence and significant energy savings.

Acknowledgements

The authors thank to Bansathali Vidhyapith, Banashtali, Rajasthan (India) for providing XRD data and USIC, University of Rajasthan, Jaipur, Rajasthan (India), for obtaining SEM measurements.

Author contributions

All the authors contributed to the original study conceptualization and design. Material synthesis, data collection, analysis and manuscript writing have been performed by [MKG], writing and sample preparation [AK], characterization and data interpretations [SK], data analysis [JN], data collection and interpretation [BLC], data analysis, editing and reviewing [SND] and writing, editing, review and supervision [RKS]. The final manuscript has been read and approved by all authors.

Funding

This research has not been financially supported.

Data availability

On request, data will be made available.

Declarations

Competing interest The authors state that they have no personal or financial conflicts that would have appeared to have impacted the research provided in this study.

References

1. S.A. Wolf, D.D. Awschalom, R.A. Buhrman, J.M. Daughton, S.V. Molnar, M.L. Roukes, A.Y. Chtchelkanova, D.M. Treger, Spintronics: a spin-based electronics vision for the future. *Science* **294**(5546), 1488–1495 (2001)
2. I. Zutic, J. Fabian, S.D. Sarma, Spintronics: fundamentals and applications. *Rev. Mod. Phys.* **76**(2), 323 (2004)
3. K. Ando, Magneto-optical studies of s, p-d exchange interactions in GaN: Mn with room-temperature ferromagnetism. *Appl. Phys. Lett.* **82**(1), 100–102 (2003)
4. K. Ueda, H. Tabata, T. Kawai, Magnetic and electric properties of transition-metal-doped ZnO films. *Appl. Phys. Lett.* **79**(7), 988–990 (2001)
5. M. Zhu, Z. Zhang, M. Zhong, M. Tariq, Y. Li, W. Li, H. Jin, K. Skotnicova, Y. Li, Oxygen vacancy induced ferromagnetism in Cu-doped ZnO. *Ceram. Int.* **43**(3), 3166–3170 (2017). <https://doi.org/10.1016/j.ceramint.2016.11.137>
6. P. Singh, R. Kumar, R.K. Singh, Progress on Transition Metal-Doped ZnO Nanoparticles and Its Application. *Ind. Eng. Chem. Res.* **58**(37), 17130–17163 (2019)
7. H. Pan, Y. Zhang, Y. Hu, H. Xie, Effect of cobalt doping on optical, magnetic and photocatalytic properties of ZnO nanoparticles. *Optik* (2020). <https://doi.org/10.1016/j.jleleo.20.164560>
8. D. More, C. Phadnis, S. Basu, A. Pathak, I. Dubenko, N. Ali, S.N. Jha, D. Bhattacharyya, S. Mahamuni, Correlation of structural and magnetic properties of Ni-doped ZnO nanocrystals. *J. Phys. D Appl. Phys.* **47**(4), 045308 (2014)
9. Z.N. Kayani, S. Iram, R. Rafi, S. Riaz, S. Naseem, Effect of Cu doping on the structural, magnetic and optical properties of ZnO thin films. *Appl. Phys. A* (2018). <https://doi.org/10.1007/s00339-018-1886-9>
10. V. Bhosle, A. Tiwari, J. Narayan, Electrical properties of transparent and conducting Ga doped ZnO. *J. Appl. Phys.* **100**(3), 033713 (2006)
11. A.K. Keshari, P. Gupta, M. Singh, ZnO nanoparticles doping with transition metal elements in polymeric and biomacromolecular matrix and their optical evolution. *Opt. Mater.* **111**, 110697 (2021)
12. T.S. Heng, S.P. Lau, S.F. Yu, H.Y. Yang, L. Wang, M. Tanemura, J.S. Chen, Magnetic anisotropy in the ferromagnetic Cu-doped ZnO nanoneedles. *Appl. Phys. Lett.* **90**(3), 032509 (2007)
13. L.N. Tong, X.M. He, H.B. Han, J.L. Hu, A.L. Xia, Y. Tong, Effects of H₂ annealing on ferromagnetism of Ni-doped ZnO powders. *Solid State Commun.* **150**(25–26), 1112–1116 (2010)
14. R. Lardé, E. Talbot, P. Pareige, H. Bieber, G. Schmerber, S. Colis, V.P. Bohnes, A. Dinia, Evidence of superparamagnetic co clusters in pulsed laser deposition-grown Zn_{0.9}Co_{0.1}O thin films using atom probe tomography. *J. Am. Chem. Soc.* **133**(5), 1451–1458 (2011)

15. D. Gao, Z. Zhang, Y. Li, B. Xia, S. Shi, D. Xue, Abnormal room temperature ferromagnetism in CuO–ZnO heterostructures: interface related or not? *Chem. Commun.* **51**, 1151–1153 (2015)
16. R. Heinhold, H.S. Kim, F. Schmidt, H.V. Wenckstern, M. Grundmann, R. Mendelsberg, R.J. Reeves, S.M. Durbin, M.W. Allen, Optical and defect properties of hydrothermal ZnO with low lithium contamination. *Appl. Phys. Lett.* **101**(6), 062105 (2012)
17. T. Dietl, H. Ohno, F. Matsukura, J. Cibert, D. Ferrand, Zener model description of ferromagnetism in zinc-blende magnetic semiconductors. *Science* **287**(5455), 1019–1022 (2000)
18. Y. Köseoğlu, Rapid synthesis of room temperature ferromagnetic Fe and Co co-doped ZnO DMS nanoparticles. *Ceram. Int.* **41**(9), 11655–11661 (2015)
19. G. Tang, X. Shi, C. Huo, Z. Wang, Room temperature ferromagnetism in hydrothermally grown Ni and Cu co-doped ZnO nanorods. *Ceram. Int.* **39**(5), 4825–4829 (2013)
20. G. Srinet, P. Varshney, R. Kumar, V. Sajal, P.K. Kulriya, M. Knobel, S. Sharma, Structural, optical and magnetic properties of Zn_{1-x}CoxO prepared by the sol–gel route. *Ceram. Int.* **39**(6), 6077–6085 (2013)
21. N. Doğan, A. Bingölbali, L. Arda, Preparation, structure and magnetic characterization of Ni doped ZnO nano-particles. *J. Magn. Magn. Mater.* **373**, 226–230 (2015)
22. L.M. Huang, A.L. Rosa, R. Ahuja, Ferromagnetism in Cu-doped ZnO from first-principles theory. *Phys. Rev. B* **74**(7), 075206 (2006)
23. M. Ferhat, A. Zaoui, R. Ahuja, Magnetism and band narrowing in Cu-doped ZnO. *Appl. Phys. Lett.* **94**(14), 142502 (2009)
24. G.A. Ali, M.E. Ismail, M.E. Hagary, E.R. Shaaban, S.H. Moustafa, M.I. Amer, H. Shaban, Optical and microstructural characterization of nanocrystalline Cu doped ZnO diluted magnetic semiconductor thin film for optoelectronic application. *Opt. Mat.* (2021). <https://doi.org/10.1016/j.optmat.2021.111312>
25. P.K. Sharma, R.K. Dutta, A.C. Paney, Doping dependent room-temperature ferromagnetism and structural properties of dilute magnetic semiconductor ZnO: Cu²⁺ nanorods. *J. Magn. Magn. Mater.* **321**(24), 4001–4005 (2009)
26. O.A. Yıldırım, C. Durucan, Room temperature synthesis of Cu incorporated ZnO nanoparticles with room temperature ferromagnetic activity: Structural, optical and magnetic characterization. *Ceram. Int* **42**(2B), 3229–3238 (2016)
27. Z. Wang, W. Xiao, M. Tian, N. Qin, H. Shi, X. Zhang, W. Zha, J. Tao, J. Tian, Effects of copper dopants on the magnetic property of lightly Cu-Doped ZnO nanocrystals. *Nanomaterials* **10**(8), 1578 (2020). <https://doi.org/10.3390/nano10081578>
28. K.C. Verma, R.K. Kotnala, Understanding lattice defects to influence ferromagnetic order of ZnO nanoparticles by Ni, Cu, Ce ions. *J. Solid State Chem.* **246**, 150–159 (2017)
29. M.H. Kane, M. Strassburg, A. Asghar, Q. Song, S. Gupta, J. Senawiratne, C. Hums, U. Haboek, A. Hoffmann, D. Azamat, W. Gehlhoff, N. Dietz, Z.J. Zhang, C.J. Summers, I.T. Ferguson, Multifunctional III-nitride dilute magnetic semiconductor epilayers and nanostructures as a future platform for spintronic devices. *Proc. SPIE* **5732**, 389 (2005). <https://doi.org/10.1117/12.582980>
30. R.A. Zargar, M. Arora, R.A. Bhat, Study of nanosized copper-doped ZnO dilute magnetic semiconductor thick films for spintronic device applications. *Appl. Phys A* (2018). <https://doi.org/10.1007/s00339-017-1457-5>
31. R. Asih, D.A. Daratika, F. Astuti, M.A. Baqiya, I. Watanabe, C. Saiyasombat, M. Kato, Y. Koike, A. Rusydi, Darminto, Enhanced ferromagnetism in Cu-Substituted ZnO nanoparticles. *Mat. Chem. Phys.* (2022). <https://doi.org/10.1016/j.matchemphys.2021.125606>
32. B.C. Joshi, A.K. Chaudhri, Sol–gel-derived Cu-doped ZnO thin films for optoelectronic applications. *ACS Omega* **7**, 21877–21881 (2022)
33. A.A. Othman, M.A. Ali, E.M.M. Ibrahim, M.A. Osman, Influence of Cu doping on structural, morphological, photoluminescence, and electrical properties of ZnO nanostructures synthesized by ice-bath assisted sonochemical method. *J. Alloys Compd.* **683**, 399e411 (2016)
34. O. Alev, N. Sarıca, O. Ozdemir, L.Ç. Arslan, S. Büyükköse, Z.Z. Öztürk, Cu-doped ZnO nanorods based QCM sensor for hazardous gases. *J. Alloys Compd.* (2020). <https://doi.org/10.1016/j.jallcom.2020.154177>
35. L. Ye, W. Guan, C. Lu, H. Zhao, X. Lu, Fabrication of hollow ZnO hexahedral nanocrystals grown on Si (100) substrate by a facile route. *Mater. Lett.* **118**, 115–118 (2014)
36. S. Zhang, B. Cheng, Z. Jia, Z. Zhao, X. Jin, Z. Zhao, G. Wu, The art of framework construction: hollow-structured materials toward high-efficiency electromagnetic wave absorption. *Adv. Compos. Hybrid Mat.* (2022). <https://doi.org/10.1007/s42114-022-00514-2>
37. D. Lan, H. Zhou, H. Wu, A polymer sponge with dual absorption of mechanical and electromagnetic energy. *J. Colloid Interface Sci.* **633**, 92–101 (2023). <https://doi.org/10.1016/j.jcis.2022.11.102>
38. H. Liang, L. Zhang, H. Wu, Exploration of twin-modified grain boundary engineering in metallic copper predominated

- electromagnetic wave absorber. *Nano-Micro small* (2022). <https://doi.org/10.1002/sml.202203620>
39. H. Liang, H. Xing, M. Qin, H. Wu, Bamboo-like short carbon fibers@Fe₃O₄@phenolic resin and honeycombl like short carbon fibers @ Fe₃O₄ @ FeO composites as high-performance electromagnetic wave absorbing materials. *Compos. Part A* (2020). <https://doi.org/10.1016/j.compositesa.2020.105959>
 40. N. Chaithanatkun, K. Onlaor, B. Tunhoo, The influence of annealing temperature on structural properties of zinc oxide nanoparticles synthesized by precipitation method. *Key Eng. Mat.* **728**, 215–220 (2017)
 41. E.H. Kisi, M.M. Elcombe, u parameters for the wurtzite structure of ZnS and ZnO using powder neutron diffraction. *Acta Crystallogr. C* **45**(12), 1867–1870 (1989). <https://doi.org/10.1107/S0108270189004269>
 42. R.S. Ganesh, E. Durgadevi, M. Navaneethan, VLd. Patil, S. Ponnusamy, C. Muthamizhchelvan, S. Kawasaki, P.S. Patil, Y. Hayakawa, Tuning the selectivity of NH₃ gas sensing response using Cu-doped ZnO nanostructures. *Sensors Actuators A: Phys.* **269**(1), 331–341 (2018). <https://doi.org/10.1016/j.sna.2017.11.042>
 43. S. Singhal, J. Kaur, T. Namgyal, R. Sharma, Cu-doped ZnO nanoparticles: Synthesis, structural and electrical properties. *Physica B* **407**(8), 1223–1226 (2012)
 44. B.H. Toby, R factors in Rietveld analysis: how good is good enough? *Powder Diffr* **21**(1), 67–70 (2006). <https://doi.org/10.1154/1.2179804>
 45. G.R. Khan, Crystallographic, structural and compositional parameters of Cu-ZnO nanocrystallites. *Appl Phys A* **126**(4), 311 (2020)
 46. Y. Liu, H. Liang, L. Xu, J. Zhao, J. Bian, Y. Luo, Y. Liu, W. Li, G. Wu, G. Du, Cu, Related doublets green band emission in ZnO: Cu thin films. *J. Appl. Phys.* (2010). <https://doi.org/10.1063/13516459>
 47. M. Öztas, M. Bedir, Thickness dependence of structural, electrical and optical properties of sprayed ZnO: Cu films. *Thin Solid Films* **516**, 1703–1709 (2008)
 48. C. Prabakar, S. Muthukumaran, V. Raja, Investigation on microstructure, energy gap, photoluminescence and magnetic studies of Co and Cu in situ doped ZnOnanostructures. *J. Mater. Sci.: Mater. Electron.* **32**(7), 9702–9720 (2021)
 49. J.H. Park, Y.J. Lee, J.S. Bae, B.S. Kim, Y.C. Cho, C. Moriyoshi, Y. Kuroiwa, S. Lee, S.Y. Jeong, Analysis of oxygen vacancy in Co-doped ZnO using the electron density distribution obtained using MEM. *Nanoscale Res. Lett.* (2015). <https://doi.org/10.1186/s11671-015-0887-2>
 50. A. Matei, V. Țucureanu, M.C. Popescu, C. Romani, I. Mihalache, Influence of Cu dopant on the morpho-structural and optical properties ZnO nanoparticles. *Ceram. Int.* **45**, 10826–10833 (2019)
 51. M. Claros, M. Setka, Y.P. Jimenez, S. Vallejos, AACVD synthesis and characterization of iron and copper oxides modified ZnO structured films. *Nanomaterials* **10**(3), 471 (2020)
 52. B. Ghosh, S.C. Ray, M. Pontsho, S. Sarma, D.K. Mishra, Y.F. Wang, W.P. Pong, A.M. Strydom, Defect induced room temperature ferromagnetism in single crystal, poly-crystal, and nanorod ZnO: A comparative study. *J. Appl. Phys.* **123**(16), 161507 (2018)
 53. R. Khokhra, B. Bharti, H.N. Lee, R. Kumar, Visible and UV photo-detection in ZnO nanostructured thin films via simple tuning of solution method. *Sci. Rep.* **7**, 15032 (2017)
 54. D.K. Mishra, P. Kumar, M.K. Sharma, J. Das, S.K. Singh, B.K. Roul, S. Varma, R. Chatterjee, V.V. Srinivasu, D. Kanjilal, Ferromagnetism in ZnO single crystal. *Physica B: Condens. Matter* (2010). <https://doi.org/10.1016/j.physb.2010.03.047>
 55. S. Pati, S.B. Majumder, P. Banerji, Role of oxygen vacancy in optical and gas sensing characteristics of ZnO thin films. *J. Alloy. Compd.* **541**, 376–379 (2012). <https://doi.org/10.1016/j.jallcom.2012.07.014>
 56. G. Vijayaprasath, R. Murugan, T. Mahalingam, Y. Hayakawa, G. Ravi, Preparation of highly oriented Al: ZnO and Cu/Al: ZnO thin films by sol-gel method and their characterization. *J. Alloy. Compd.* **649**, 275–284 (2015)
 57. K. Noipa, S. Rujirawat, R. Yimnirun, V. Promarak, S. Maensiri, Synthesis, structural, optical and magnetic properties of Cu-doped ZnO nanorods prepared by a simple direct thermal decomposition route. *Appl. Phys. A* **117**(2), 927–935 (2014). <https://doi.org/10.1007/s00339-014-8475-3>
 58. A. Azam, A.S. Ahmed, M.S. Ansari, M. Shafeeq, A.H. Naqvi, Study of electrical properties of nickel doped SnO₂ ceramic nanoparticles. *J. Alloy. Compd.* **506**(1), 237–242 (2010)
 59. M.L. Singla, M. Shafeeq, M. Kumar, Optical characterization of ZnO nanoparticles capped with various surfactants. *J. Lumin.* **129**(12), 434–438 (2009). <https://doi.org/10.1016/j.jlumin.2008.11.021>
 60. A.J. Reddy, M.K. Kokila, H. Nagabhushana, R.P.S. Chakradhar, C. Shivakumar, J.L. Rao, B.M. Nagabhushana, Structural, optical and EPR studies on ZnO: Cu nanopowders prepared via low temperature solution combustion synthesis. *J. Alloy. Compd.* **509**(17), 5349–5355 (2011). <https://doi.org/10.1016/j.jallcom.2011.02.043>
 61. D. Anbuselvan, S. Muthukumaran, Defects related microstructure, optical and photoluminescence behavior of Ni, Cu co-doped ZnO nanoparticles by Co-precipitation method. *Opt. Mater.* **42**, 124–131 (2015)

62. S. Anandan, S. Muthukumar, M. Ashokkumar, Structural and optical properties of Y, Cu co-doped ZnO nanoparticles by sol-gel method. *Superlattices Microstruct.* **74**, 247–260 (2014)
63. R. Bhardwaj, A. Bharti, J.P. Singh, K.H. Chae, N. Goyal, Influence of Cu doping on the local electronic and magnetic properties of ZnO nanostructures. *Nanoscale-Advanc* (2020). <https://doi.org/10.1039/d0na00499e>
64. S. Suwanboon, P. Amornpitoksuk, P. Bangrak, A. Sukolrat, N. Muensit, The dependence of optical properties on the morphology and defects of nanocrystalline ZnO powders and their antibacterial activity. *J. Ceram. Process. Res.* **11**(5), 547–551 (2010)
65. M. Sajjad, I. Ullaha, M.I. Khanb, J. Khanc, M.Y. Khana, M.T. Qureshi, Structural and optical properties of pure and copper doped zinc oxide nanoparticles. *Results Phys.* **9**, 1301–1309 (2018). <https://doi.org/10.1016/j.rinp.2018.04.010>
66. A.I. Istrate, I. Mihalache, C. Romanitan, O. Tutunaru, R. Gavrilă, V. Dediu, Copper doping effect on the properties in ZnO films deposited by sol–gel. *J Mater Sci: Mater Electron* **32**, 4021–4033 (2021)
67. S. Kuriakose, B. Satpati, S. Mohapatra, Highly efficient photocatalytic degradation of organic dyes by Cu doped ZnO nanostructures. *Phys. Chem. Chem. Phys.* **17**, 25172 (2015). <https://doi.org/10.1039/c5cp01681a>
68. B. Lin, Z. Fua, Green luminescent center in undoped zinc oxide films deposited on silicon substrates. *Appl. Phys. Lett.* **79**, 943–945 (2001)
69. X. Peng, J. Xu, H. Zang, B. Wang, Z. Wang, Structural and PL properties of Cu-doped ZnO films. *J. Lumin.* **128**(3), 297–300 (2008)
70. T. Gao, G. Meng, Y. Tian, S. Sun, X. Liu, L. Zhang, Photoluminescence of ZnO nanoparticles loaded into porous anodic alumina hosts. *J. Phys.: Condens. Matter* **14**(7), 12651–12656 (2002)
71. B.J. Kwon, J.Y. Kim, S.M. Choi, S.J. An, Highly transparent and conducting graphene-embedded ZnO films with enhanced photoluminescence fabricated by aerosol synthesis. *Nanotechnology* **25**, 085701 (2014)
72. S. Dhara, P.K. Giri, Improved fast photoresponse from Al doped ZnO nanowires network decorated with Au nanoparticles. *Chem. Phys. Lett.* **541**, 39–43 (2012)
73. C.R. Michea, M. Morel, F. Gracia, G. Morell, E. Mosquera, Influence of copper doping on structural, morphological, optical, and vibrational properties of ZnO nanoparticles synthesized by sol gel method. *Surf. Interfaces* **21**, 100700 (2020)
74. J.P. Singh, K.H. Chae, d0 Ferromagnetism of magnesium oxide. *Matter. Condens.* (2017). <https://doi.org/10.3390/condmat2040036>
75. S. Krishnamurthy, C.M. Guinness, L.S. Dorneles, M. Venkatesan, J.M.D. Coey, J.G. Lunney, C.H. Patterson, K.E. Smith, T. Learmonth, P.A. Glans, J.H. Guo, Soft-X-ray spectroscopic investigation of ferromagnetic Co-doped ZnO. *J. Appl. Phys.* **99**(08), M111 (2006)
76. J.M.D. Coey, M. Venkatesan, C.B. Fitzgerald, Donor impurity band exchange in dilute ferromagnetic oxides. *Nat. Mater.* **4**, 173–179 (2005)
77. J.E. Jaffe, T.C. Droubay, S.A. Chambers, Oxygen vacancies and ferromagnetism in $\text{Co}_x\text{Ti}_{1-x}\text{O}_{2-x-y}$. *J. Appl. Phys.* **97**, 073908–073910 (2005). <https://doi.org/10.1063/1.1868056>
78. W. Yan, Z. Sun, Z. Pan, Q. Liu, T. Yao, Z. Wu, C. Song, F. Zeng, Y. Xie, T. Hu, S. Wei, Oxygen vacancy effect on room-temperature ferromagnetism of rutile Co: TiO₂ thin films. *Appl. Phys. Lett.* **94**, 042508–042510 (2009). <https://doi.org/10.1063/1.3075844>
79. K.G. Roberts, M. Varela, S. Rashkeev, S.T. Pantelides, S.J. Pennycook, K.M. Krishnan, Defect-mediated ferromagnetism in insulating Co-doped anatase TiO₂ thin films. *Phys. Rev. B* **78**(1), 014409–0140914 (2008). <https://doi.org/10.1103/PhysRevB.78.014409>
80. K.A. Griffin, A.B. Pakhomov, C.M. Wang, S.M. Heald, K.M. Krishnan, Interionic ferromagnetism in insulating cobalt doped anatase TiO₂. *Phys. Rev. Lett.* **94**(15), 157204–157207 (2005). <https://doi.org/10.1103/PhysRevLett.94.157204>
81. W. Liu, X. Tang, Z. Tang, F. Chu, T. Zeng, N. Tang, Role of oxygen defects in magnetic property of Cu doped ZnO. *J. Alloy. Compd.* **615**, 740–744 (2014)
82. Z. Ma, F. Ren, X. Ming, Y. Long, A.A. Volinsky, Cu-doped ZnO electronic structure and optical properties studied by first-principles calculations and experiments. *Materials* **12**(1), 196 (2019)
83. N.M.A. Hadia, M. Aljudai, M. Alzaid, S.H. Mohamed, W.S. Mohamed, Synthesis and characterization of undoped and copper-doped zinc oxide nanowires for optoelectronic and solar cells applications. *Appl. Phys. A* (2022). <https://doi.org/10.1007/s00339-021-05155-8>
84. D.L. Hou, X.J. Ye, H.J. Meng, H.J. Zhou, X.L. Li, C.M. Zhen, G.D. Tang, Magnetic properties of n-type Cu-doped ZnO thin films. *Appl. Phys. Lett.* **90**(14), 142502 (2007)
85. Y. Chen, X. Xu, X. Li, G. Zhang, Vacancy induced room temperature ferromagnetism in Cu-doped ZnO nanofibers. *Appl. Surf. Sci.* **506**, 144905 (2020)

86. P.S. Vachhani, G. Dalba, R.K. Ramamoorthy, F. Rocca, O. Šipr, A.K. Bhatnagar, Cu doped ZnO pellets: study of structure and Cu specific magnetic properties. *J. Phys. Cond. Mat.* **24**(50), 506001 (2012)
87. X. Qing-Yu, Z. Xiao-Hong, G. You-Pin, Paramagnetism in Cu-doped ZnO. *Chin. Phys. B* **19**(7), 077501 (2010)
88. Q. Wang, J. Wang, X. Zhong, Q. Tan, Y. Zhou, The magnetic phase transition in Cu-doped ZnO: From bulk to nanocluster. *Solid State Commun.* **152**(1), 50–52 (2012)

Publisher's Note Springer Nature remains neutral with regard to jurisdictional claims in published maps and institutional affiliations.

Springer Nature or its licensor (e.g. a society or other partner) holds exclusive rights to this article under a publishing agreement with the author(s) or other rightsholder(s); author self-archiving of the accepted manuscript version of this article is solely governed by the terms of such publishing agreement and applicable law.